Journal of Thermal Analysis and Calorimetry (2021) 146:1405–1420
https://doi.org/10.1007/s10973-020-10462-y

Thermokinetic and thermodynamics of Pechini derived $Li_{7-3x}Al_xLa_3Zr_2O_{12}$ (X = 0.0–0.2) xerogel decomposition under oxidative conditions

Gamzenur Özsin[1] · **Kamil Burak Dermenci**[2] · **Servet Turan**[2]

Received: 14 January 2020 / Accepted: 1 December 2020 / Published online: 5 January 2021

Abstract

Solid electrolytes for all-solid-state Li-ion batteries have attracted significant interest with their outstanding safety. But their poor ionic conductivity limits their widespread use. $Li_7La_3Zr_2O_{12}$ solid electrolytes have the potential of showing comparable ionic conductivities with commercially available electrolytes. However, its high ion conductive cubic phase is not stable at room temperature. Studies demonstrated that the cubic $Li_7La_3Zr_2O_{12}$ phase can be stabilized easier than solid-state method by modified Pechini method and very little work has been done in order to understand what makes the phase transformation easier. For this purpose, thermal decomposition behavior, model-free kinetics and thermodynamics of $Li_7La_3Zr_2O_{12}$ xerogels synthesized by modified Pechini method were investigated and the effect of stabilizer (Al) addition was discussed in this study. The results showed the presence of four peak zones and the main reaction zone includes multiple reactions. Different statistical functions were tested for deconvolution of main reaction zone and the best fits were obtained by Bigaussian and Asym2sig statistical functions. The multiple reactions in the main thermal degradation zone were separated into three reaction zones and thermokinetic and thermodynamic calculations were employed using model-free approach. The results also showed that Al incorporation expanded the main thermal decomposition zone of LLZO and resulted in changes in kinetic and thermodynamic parameters.

Keywords $Li_7la_3zr_2O_{12}$ · Sol–gel · Kinetic · Non-isothermal · Thermodynamics

List of Symbols

Symbol	Meaning
A	Pre-exponential factor (s^{-1})
E_a	Activation energy (kJ mol^{-1})
h	Planck constant (6.626×10^{-34} J s).
K_B	Boltzmann constant (1.381×10^{-23} J K^{-1})
R	Universal gas constant (8.3144×10^{-3} kJ mol^{-1} K^{-1})
t	Time (s)
T	Temperature (K)
T_m	Temperature at the maximum conversion rate (K)
w_t	Mass at time t (mg)
w_o	Mass at the initial stage of the reaction (mg)
w_f	Mass at the final stage of the reaction (mg)
α	Conversion degree
β	Heating rate (K min^{-1})
$\bar{x}$	Mean value
$k(T)$	Temperature function
$f(\alpha)$	Reaction model function
$g(\alpha)$	Integrated form of reaction model
$p(u)$	Temperature integral
ΔG	Gibbs free energy change (kJ mol^{-1})
ΔH	Enthalpy change (kJ mol^{-1})
ΔS	Entropy change (J mol^{-1} K^{-1})

Introduction

Li-ion batteries cover the important portion on the worldwide battery market because of their outstanding energy and power densities, long lifetime and better rate capabilities [1]. However, their toxic and flammable organic-based liquid electrolytes concern the safe use and recycling of these batteries in critical applications such as electrical vehicles [2]. Therefore, safety issues due to highly flammable

---

✉ Kamil Burak Dermenci
kbdermenci@eskisehir.edu.tr

[1] Department of Chemical Engineering, Faculty of Engineering, Bilecik Şeyh Edebali University, 11230 Bilecik, Turkey

[2] Department of Materials Science and Engineering, Faculty of Engineering, Eskişehir Technical University, 26555 Eskisehir, Turkey

organic-based liquid electrolyte component are considered a top priority especially for these applications [3–5]. Accordingly, researches on safer solid electrolytes have been rapidly increased, especially within the last decade [6, 7]. Therefore, a great deal of interest lies in the development of solid electrolytes which are prominent candidates for overcoming the safety issues for Li-ion batteries. The key features of solid electrolytes can be summarized [8]:

- *High thermal stability*: It can be reached higher operating temperatures compared to liquid electrolytes
- *High electrochemical stability window*: Solid electrolytes' high electrochemical stability window utilizes high voltage cathodes providing more power density.
- *No solid-electrolyte interface (SEI) formation*: Undesired reaction products cannot be formed at the electrode–electrolyte interface during cycling.
- *Suppressed Li dendrite formation*: Li dendrite formation and propagation through solid electrolyte is largely confined.

On the other hand, some of the important drawbacks can be pointed out:

- *Transport properties*: Solid electrolytes show relatively low ionic conductivity that hinders to operate high C-rates.
- *Contact/interface resistance*: The interfacial resistance of electrode–electrolyte interface is high due to poor wetting of electrodes on the electrolyte.
- *Environmental stability*: Wide variety of solid electrolytes are air and humidity sensitive compounds and their properties strictly depend on environmental conditions.

Garnet type $Li_7La_3Zr_2O_{12}$ (LLZO) with cubic crystal structure shows a great potential to overcome the drawbacks mentioned above. It shows fairly high ionic conductivity and very low interfacial resistance. Besides, excellent stability against air and humidity makes LLZO a widely studied solid electrolyte [9]. However, LLZO having a cubic crystal structure is the high temperature stable phase of LLZO [10] and needs to be stabilized at room temperature. For this purpose, several approaches have been done. Firstly, it has been reported that stabilizers such as Al, Ga, Ta and Fe was added into the structure. They not only act as a stabilizer to stabilize cubic LLZO phase at room temperature but also enhance ionic conductivity by creating lattice defects [11–14]. Secondly, synthesis methods could tune the cubic phase stabilization conditions.

The common synthesis methods of LLZO are the solid-state reaction method which is based on diffusion of species between precursors and the modified Pechini method which forms organic complexes of metal ions in a 3D network [15, 16]. The solid-state reaction of garnet type LLZO is a time-consuming process because it requires relatively high synthesis temperatures and time to complete cubic phase stabilization. In order to prevent extensive Lithium losses during high temperature and long-lasting synthesis process, powder-bed sintering is commonly used in solid-state reaction method. As a result of the powder-bed synthesis, relatively low cubic LLZO phase production yield was observed since most of the powders is consumed by powder bed construction. In addition to that, the obtained product is in the form of pellet. If cubic LLZO phase is needed in a powder form, additional pellet grinding should be done [17–19].

It was recently shown by our group that the modified Pechini method could be the option to obtain the high purity cubic LLZO powders in a relatively shorter heat treatment time with high production yield [20] compared to the solid-state reaction method [19]. The reason behind this can be attributed to the decomposition kinetics and thermodynamics of organic complexes in the modified Pechini method [21]. Although the modified Pechini method is very popular among LLZO synthesis methods, there is no research focusing on the thermal decomposition kinetics and thermodynamics during LLZO synthesis, to the best of our knowledge. Considering the complexities involved in the kinetics of the reactions taking place during LLZO synthesis, this study firstly investigates the thermal decomposition kinetics of LLZO by using model-free approaches. For this purpose, the thermal decomposition kinetics are discussed by using different model-free kinetic models. The effect of stabilizer (Al) addition on both thermal decomposition kinetics and thermodynamic parameters are also reported based on thermogravimetric analysis (TGA).

Experimental

Experimental methodology

A modified Pechini method was used to obtain LLZO xerogels having up to 0.2 mol% Al addition. Stochiometric amounts of $LiNO_3$ (Merck), $La(NO_3)_3{\cdot}6H_2O$ (Alfa Aesar), $Al(NO_3)_3{\cdot}9H_2O$ (Sigma-Aldrich) and $ZrOCl_2{\cdot}8H_2O$ (Merck) was dissolved in the deionized water until a transparent solution was reached. 15 mass% of excess lithium as $LiNO_3$ was added in order to compensate Li losses during high temperature heat treatment. Then, the resulting solution was heated to 393 K under moderate stirring conditions for gelation. After the gelation, the obtained white precipitates were dried at 423 K for 12 h. Brownish dried powders (referred as xerogel) were then milled for 30 min (Retsch RM200) by using agate mortar and pestle. The procedure was also described in our previous paper [20].

Thermal analysis was conducted by using SDT-Q600 (TA Instruments). For each experiment, approximately 10 mg of sample was loaded in alumina crucible and heated up to 1273 K at different heating rates of 5, 10, 20 and 40 K min^{-1} in a non-isothermal mode. All measurements were conducted under air atmosphere with a flow rate of 100 cm^3 min^{-1}. The collected data from TGA was used for further kinetic and thermodynamic analyses.

Kinetic analysis

The fundamentals of kinetic analysis of thermal conversion based on that the rate depends on the concentration of reactants and temperature (T). In the case of linear heating rates ($\beta = \mathrm{d}T/\mathrm{d}t$, t = time), two functions, namely temperature function [$k(T)$] and fractional conversion function [f(α)] specify kinetic expression as given in Eq. 1:

$$\frac{\mathrm{d}\alpha}{\mathrm{d}t} = \beta\frac{\mathrm{d}\alpha}{\mathrm{d}T} = k(T)f(\alpha) \tag{1}$$

The conversion degree (α) for certain temperature is expressed as given in Eq. 2:

$$\alpha = \frac{w_o - w_t}{w_o - w_f} \tag{2}$$

where; w_t is the sample mass at time t or temperature T, and w_o and w_f are the sample masses at the initial and final stages of the reaction, respectively. TGA is considered as a suitable experimental method to determine conversion degree and investigate the kinetics of thermal decomposition under controlled heating rate and atmosphere [22, 23]. Rate constant is mainly dependent on temperature and the related function is typically described by the following Arrhenius equation:

$$k(T) = A\exp\left(-\frac{E_a}{RT}\right) \tag{3}$$

where E_a is the activation energy, A is the pre-exponential factor, and R is the gas constant. Mathematical manipulation of Eqs. 1 and 3 can lead to;

$$\beta\frac{\mathrm{d}\alpha}{\mathrm{d}T} = A\exp\left(-\frac{E_a}{RT}\right)f(\alpha) \tag{4}$$

Equation (4) may also be integrated into,

$$\int_0^\alpha \frac{\mathrm{d}\alpha}{f(\alpha)} = g(\alpha) = \frac{A}{\beta}\int_{\mathrm{To}}^{T} \exp\left(-\frac{E_a}{RT}\right)\mathrm{d}T \equiv \frac{AE_a}{\beta R}p(u) \tag{5}$$

$g(\alpha)$ and $p(u)$ in Eq. (5) are known as the integrated forms of the conversion function, $f(\alpha)$, and the temperature integral, respectively. $p(u)$ function of Eq. (5) is given by:

$$p(u) = \int_\infty^u -\frac{(\exp(-u))}{u^2}\mathrm{d}u \tag{6}$$

where $u = E_a/RT$. Since $p(u)$ cannot be solved analytically, mathematical approximations may be used in order to estimate kinetic parameters by fitting the degradation of TGA. Herein, iso-conversional analysis gains importance in order to calculate the activation energy of a thermally activated reactions. Iso-conversional approach is convenient to obtain kinetic parameters without defining the exact reaction model and models based on iso-conversional approach they are referred as model-free methods [24]. These methods are based on the principle that the reaction rate is a function of temperature at any constant conversion and the reaction mechanisms are not affected by the applied temperature program [25, 26] so that;

$$\left[\frac{\mathrm{d}\ln(\mathrm{d}\alpha/\mathrm{d}t)}{\mathrm{d}T^{-1}}\right]_\alpha = -\frac{E_\alpha}{R} \tag{7}$$

A 0.1 increment in conversion degree was used to compute the E_α values, as a function of the conversion using the Friedmann, Flynn–Wall–Ozawa (FWO) and Starink methods [27–30] to observe possible step-wise nature of the degradation process. A conversion-dependent activation energy was obtained for each deconvoluted peak. For this purpose, independent overlapping decomposition reactions were separated by considering overlapping-peak signals. An analytical approach involving the deconvolution of the overlapping decomposition steps from the main thermal decomposition stage was used by the help of Gaussian, Bigaussian, Voigt, Asym2sig, Pearson and Lorentz functions. The best fitting was obtained by comparing the converged fit qualities. For the calculation of pre-exponential factor at specific conversion degree (A_α), $E_{a\alpha}$ values calculated by Friedmann method is used since the method is free from any assumption of temperature integral [31]. By applying Kissinger's equation pre-exponential factor in Arrhenius equation was calculated by:

$$A_\alpha = \frac{\beta E_\alpha \exp(E_\alpha/RT_m)}{RT_m^2} \tag{8}$$

where T_m is the temperature at the maximum conversion rate.

Thermodynamic analysis

Analogously with kinetics, thermodynamic parameters such as changes in enthalpy (ΔH), Gibbs free energy (ΔG) and entropy (ΔS) can be calculated using TGA by Eqs. (9)–(11):

$$\Delta H = E_a - RT \tag{9}$$

$$\Delta G = E_a + RT_m \ln\left(\frac{K_B T_m}{hA}\right) \tag{10}$$

$$\Delta S = \frac{\Delta H - \Delta G}{T_m} \tag{11}$$

Here, K_B is Boltzmann constant (1.381×10^{-23} J K^{-1}) and h is the Plank constant (6.626×10^{-34} J s).

Results and discussion

Thermal analysis of stabilizer-free and Al-stabilized $Li_7La_3Zr_2O_{12}$

The TG and differential thermogravimetry (dTG) curves for as-prepared stabilizer-free LLZO are given in Fig. 1 to define the oxidative characteristics of the sample.

The curves of LLZO showed that, with the increase in heating rate from 5 to 40 K min^{-1}, not only the maximum decomposition rate increased from 1.329 to 14.31% min^{-1}; but also the initial and final temperatures of the main thermal degradation zone including other minor zones shifted to higher temperatures due to the hysteresis effect. However, the thermal decomposition profiles remained nearly the same which indicate similar reaction mechanisms for all heating rates. It is known that, the sample residence time is shorter and the necessary temperature for the decomposition process is higher at higher heating rates. In the case of slower heating rates, the heat transfer period becomes higher, and hence, there is a plenty of time for the flowing gas to equalize the temperature of the sample and the furnace. On the contrary, heat transfer time to eliminate the temperature gradient between the sample and furnace decreases with an increase in the heating rate [32]. The main temperature range of the thermal decomposition of LLZO was found from 436.9 to 724.7 K, depending on the heating rate. At lower temperatures than the main degradation zone conversion led to almost 97 mass% residual mass due to removal of bound water, whereas at the main thermal decomposition zone at higher temperatures, the residual mass reached 40–45 mass% of the initial value at 5–40 K min^{-1} heating rate. Approximately, 52 mass% of the sample mass is lost during the main thermal decomposition phase pointing out the extensive gas exhaustion. A TGA/FT-IR analysis of the formed gases conducted by our group revealed in the previous paper that the exhaust gases consisted of significant amount of CO_2 and small amount of H_2O at all temperatures up to 1273 K [20]. Thus, by combining findings in the previous paper and the current findings, one can conclude that mass loss in the main thermal decomposition zone is due

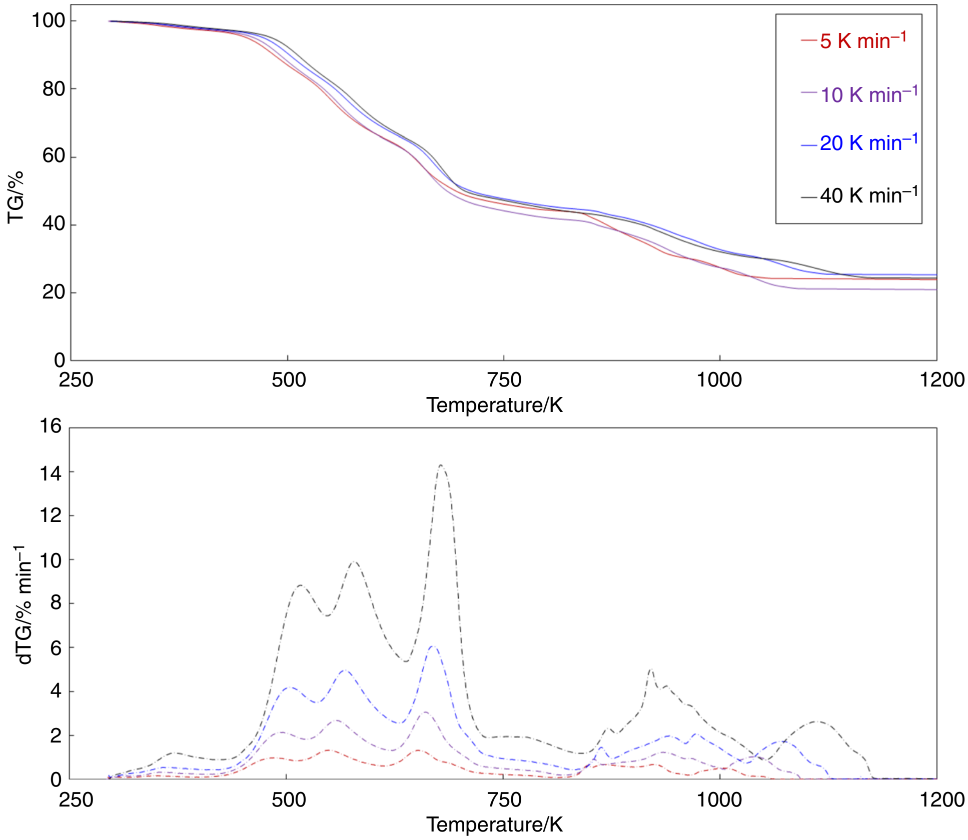

Fig. 1 TG and dTG curves of LLZO

to the removal of citric acid which was coming from the additives. After this point, CO_2 and H_2O release could be attributed to the decarboxylation and dehydration reactions during the decomposition of metal–organic complexes since it was reported that the first formations of LLZO and other metal oxides were seen at the heat treatment temperatures as low as 873 K [33]. It should also be noted that it is quite hard to identify and discriminate each decomposition zone because of the xerogel's five different element containing complex structure. The solid residue remains from this last mass loss stage includes LLZO and minor impurities such as Li_2ZrO_3, ZrO_2, $La_2Zr_2O_7$ depending on the Al content as it was explained in our previous work [20]. The curves of the Al-stabilized samples recorded at multiple heating rates are also plotted and depicted in Figs. 2 and 3.

The numerical results of the main mass loss zone during the oxidative decomposition process for all Al-free and Al-stabilized samples are summarized in Table 1.

Accordingly, Al appeared to change the peak positions as shifting all characteristic temperatures during the main thermal decomposition stage. This suggested that the decomposition of Al-incorporated LLZO follows a different mechanism than the Al-free LLZO. During thermal decomposition, the onset and offset temperatures (T_i and T_F) of the Al-free LLZO were always lower than the Al-stabilized samples over the entire temperature range, indicating that LLZO is thermally labile while LLZO-0.1Al and LLZO-0.2Al are more stable. This implies that Al-free LLZO xerogel decomposition happens at a faster rate than the decomposition of Al-stabilized LLZO.

The highest peak points in the main reaction zone which are given by T_{P1}, T_{P2} and T_{P3} also showed the effect of Al on the characteristics of the xerogel decomposition of LLZO. By increasing the Al ratio, T_{P1} was decreased when both T_{P2} and T_{P3} shifted slightly to the higher temperatures. Considering that, Al addition expanded the main thermal decomposition zone.

The subtle point that need to be pointed out is that the possibility of a single stage reaction may be ruled out for both Al-free and Al-stabilized samples. Multi-stage complex decomposition reactions identified due to the multiple overlapping dTG peaks were observed in the main thermal decomposition range for all samples.

Thermal decomposition kinetics of stabilizer-free and Al-stabilized $Li_7La_3Zr_2O_{12}$ using model-free iso-conversional approach

It is crucial to determine the kinetics of thermal decomposition of xerogels and determine the effect of Al, and thus,

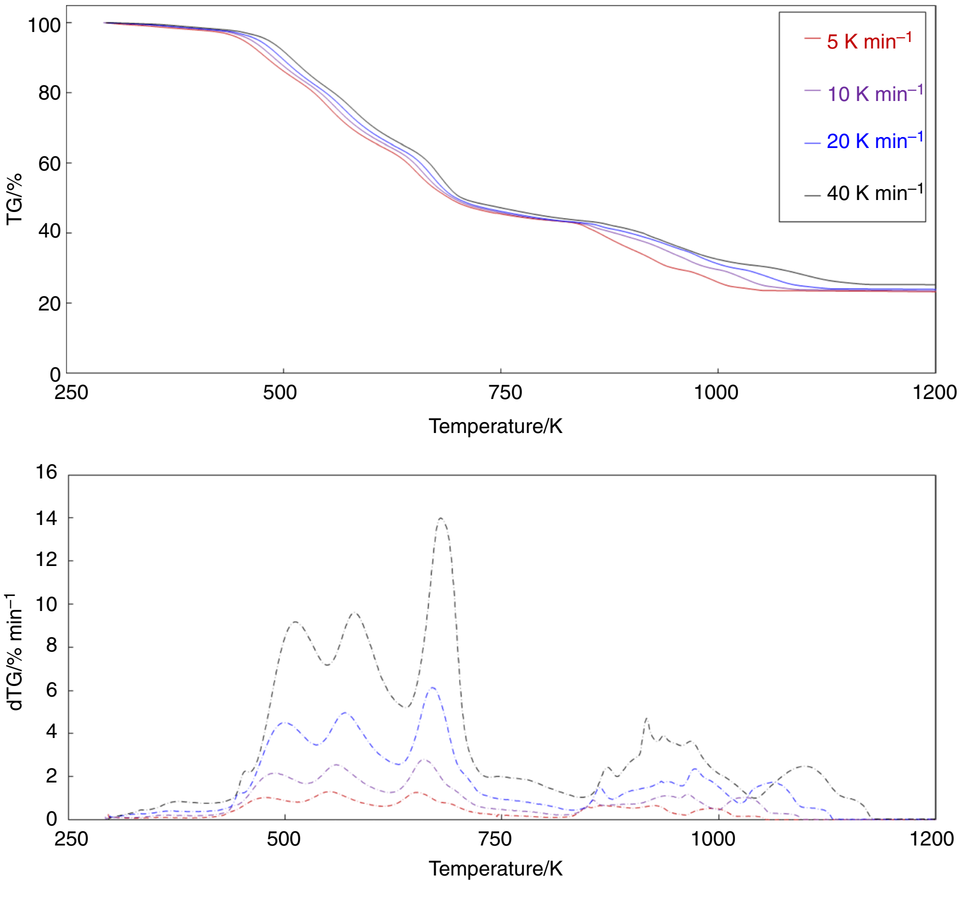

Fig. 2 TG and dTG curves of LLZO-0.1Al

Fig. 3 TG and dTG curves of LLZO-0.2Al

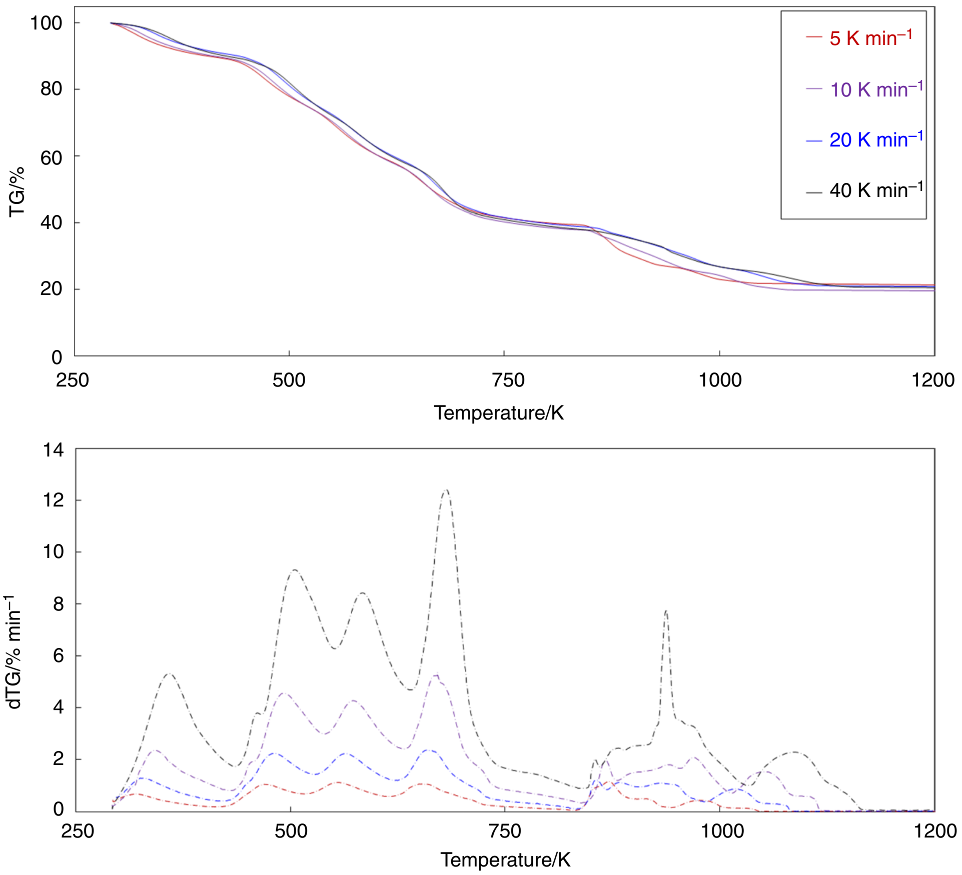

Table 1 Characteristic temperatures of main thermal decomposition zone

	β/K min^{-1}	T_i/K	T_{P1}/K	T_{P2}/K	T_{P3}/K	T_F/K
LLZO	5	437.05	485.47	547.81	651.92	717.17
	10	446.03	496.34	556.65	651.99	720.23
	20	449.47	505.50	568.32	668.91	724.36
	40	454.29	516.64	578.16	678.43	724.83
LLZO-0.1Al	5	441.26	478.05	552.44	652.55	722.3
	10	446.59	489.28	559.53	660.01	725.27
	20	453.24	498.56	569.18	669.98	731.02
	40	456.66	511.93	579.92	679.25	732.71
LLZO-0.2Al	5	441.95	469.48	558.71	654.63	730.26
	10	447.07	480.90	563.58	660.14	733.39
	20	456.79	493.29	573.20	670.42	739.03
	40	457.39	505.14	583.53	680.79	740.88

T_i: initial temperature of the main decomposition zone

T_{P1}:1st peak temperature of the main decomposition zone

T_{P2}: 2nd peak temperature of the main decomposition zone

T_{P3}: 3rd peak temperature of the main decomposition zone

T_F: final temperature of the main decomposition zone

an equivalent stage of degradation for different extent of conversions were evaluated and the values of activation energy were calculated for each conversion degree via the iso-conversional approach. The activation energy could be also described as the minimum energy required to break bonds between atoms. If the apparent activation energy has a high value, the reaction will be slow. Therefore, it is considered as a vital parameter for the reactivity and sensitivity of a reaction. The resulting activation energy-conversion degree dependencies of all samples are shown in Table 2.

The change of activation energy is shown over the conversion range of 0.1–0.9 which were obtained from the fitting of non-isothermal runs. Regarding the calculated mean values of the activation energy by the Friedman method, it can be understood that mean value for LLZO was 280.4 kJ mol^{-1}, which was slightly different than the mean activation energies of the other two kinetic methods as FWO and Starink as, respectively, 262.4 and 266.2 kJ mol^{-1}. Despite small deviations, all activation values showed similar trends on average. The differences among the kinetic models can be attributed to the equation parameters and assumptions of each method. It was determined that the activation energy values for LLZO decomposition were fully dependent on the conversion degree. The results at different conversion degrees had fairly high linear correlation coefficients, 0.9177 and 0.9997 depending on the kinetic model indicating that the estimated activation energy values satisfied the consistency of the fitting with the experimental TGA data. The variation of activation energy with conversion degree underlined the complexity of the thermal decomposition mechanisms which may include simultaneous thermal degradation reactions happening at different phases. Therefore, oxidative thermal decomposition should include several stages and the reaction chemistry of stabilizer-free LLZO seems quite complex with unknown myriad reactions such as parallel, complex and competitive reactions which is a highly temperature-dependent phenomenon [34].

Table 2 Activation energy distribution over the conversion degree for LLZO and Al-stabilized LLZO samples using iso-conversional approach/kJ mol^{-1}

	α	Friedman		FWO		Starink	
		E_a	R^2	E_a	R^2	E_a	R^2
LLZO	0.1	173.0	0.9987	155.2	0.9992	155.4	0.9991
	0.2	199.7	0.9724	193.3	0.9989	194.9	0.9988
	0.3	255.7	0.9740	240.4	0.9995	243.9	0.9995
	0.4	241.4	0.9963	224.2	0.9997	226.6	0.9997
	0.5	285.3	0.9855	236.0	0.9989	238.7	0.9988
	0.6	236.7	0.9013	271.4	0.9954	275.4	0.9951
	0.7	268.3	0.9710	335.8	0.9977	342.4	0.9976
	0.8	383.0	0.9815	329.9	0.9981	335.1	0.9980
	0.9	480.2	0.9177	375.2	0.9818	383.1	0.9809
	$\bar{x}$	280.4		262.4		266.2	
LLZO-0.1Al	0.1	173.1	0.9892	154.0	0.9992	154.2	0.9991
	0.2	220.6	0.9889	194.3	0.9967	196.0	0.9964
	0.3	285.6	0.9943	273.5	0.9988	278.7	0.9987
	0.4	231.5	0.9959	243.8	0.9996	247.2	0.9995
	0.5	239.6	0.9923	250.3	0.9997	253.7	0.9997
	0.6	255.6	0.9694	289.0	0.9990	293.8	0.9989
	0.7	378.9	0.9848	335.4	0.9993	342.0	0.9992
	0.8	399.5	0.9979	345.1	0.9988	351.8	0.9979
	0.9	406.0	0.9995	386.6	0.9849	395.0	0.9841
	$\bar{x}$	287.8		274.7		279.1	
LLZO-0.2Al	0.1	153.5	0.9806	156.5	0.9902	156.9	0.9894
	0.2	200.0	0.9637	194.6	0.9835	196.5	0.9822
	0.3	340.0	0.9681	349.7	0.9470	342.0	0.9447
	0.4	337.0	0.9535	300.6	0.9693	306.8	0.9677
	0.5	271.4	0.9808	283.6	0.9764	288.6	0.9750
	0.6	303.4	0.9347	309.1	0.9542	314.9	0.9517
	0.7	369.9	0.9634	418.6	0.9675	429.2	0.9660
	0.8	375.4	0.9555	351.9	0.9706	358.9	0.9691
	0.9	414.1	0.9737	332.3	0.9761	338.1	0.9747
	$\bar{x}$	307.2		299.7		303.6	

All applied kinetic methods produced a variable activation energy trend for the whole decomposition process and hence the complexity of the kinetics was revealed for the Al-stabilized samples. Both LLZO-0.1Al and LLZO-0.2Al oxidation process could involve several complex heterogeneous reactions and these heterogeneous conversions occur in parallel and/or sequence which causes the difference in the rates of various processes according to the fluctuations observed in activation energy with respect to the conversion degree. The activation energy calculations with the Friedman, FWO and Starink methods were found to almost overlap with similar trends, but the average values were slightly different for both Al-stabilized samples. The differences in the value of activation energy were due to data being obtained from different approaches. All in all, the oxidative thermal decomposition processes of both Al-free and Al-stabilized samples could not be described by a single-step rate equation throughout the whole range of conversion degrees and temperatures in the main decomposition zone. Various energy levels for distinct conversion degrees suggested that the process proceeded with varied reaction mechanisms and rates [35]. The progressive increase in the values of activation energy at higher conversion degrees was representative of the great variety of bonds in the LLZO matrix and the multiphasic character of thermal conversion which may have resulted in complex competitive or consecutive multi-step reactions [36].

Multi-stage kinetics of stabilizer-free and Al-stabilized $Li_7La_3Zr_2O_{12}$ using deconvolution approach

Iso-conversional approach is known to result systematic error in the activation energy when the latter strongly varies with the conversion degree. This error may be eliminated by using different approaches that properly accounts for the changes in the activation energy to perform multistage kinetic analysis. For instance, the use of multi-peak fitting method increases normally the signal resolution by a numerical calculation and mathematical algorithm, based on an appropriate function and it is especially useful to separate and analyze the overlapping peaks. Therefore, peak deconvolution approach was used to analyze main thermal degradation zone and different statistical functions were implemented to achieve best fitting with the experimental data. The results of three sub-stages peak fitting can be explained by the existence of three partial reactions during main LLZO oxidation as shown in Fig. 4. The sub-stages were abbreviated as A, B, C and kinetic analysis were enhanced considering complex multi-stage reactions in the main thermal degradation zone. According to the analyses of Al-incorporated

Fig. 4 The peak deconvolution results at different heating rates for LLZO

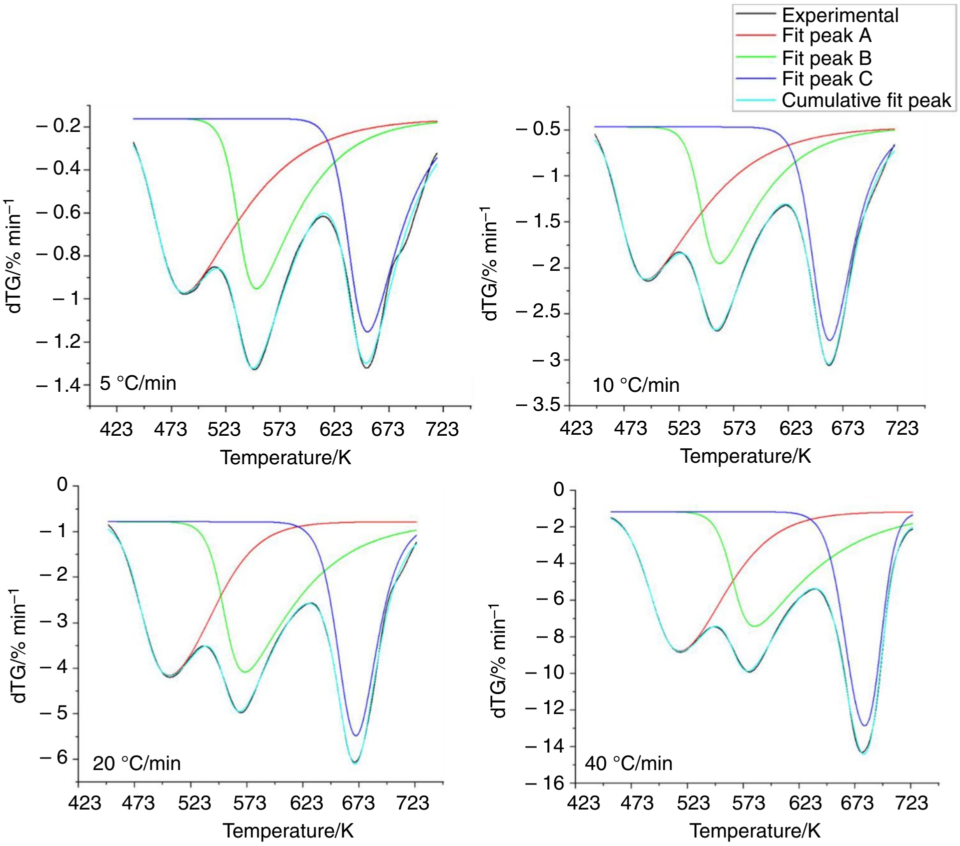

LLZO samples, number of the sub-stages were found same with the LLZO while peak positions were changing. On the basis of deconvolution approach, the separated steps for all heating rates and samples were grouped in Table 3 for all of the samples. According to the deconvolution process and statistical analysis combinations of Bigaussian and Asym2sig statistical functions seemed to be adequate for fitting dTG curves, while the Gaussian, Lorentz, Pearson and Voight could not show satisfactory converge with the experimental data. The results of peak analyses had fairly high linear correlation coefficients between 0.9890 and 0.9991 indicating that the separated peaks and cumulates satisfied the consistency of the fitting with the experimental data.

Table 3 Characteristic temperatures of deconvoluted peaks at main thermal decomposition zone

Sample	β/K min^{-1}	Peak A			Peak B			Peak C			Adj. R^2
		T_{Ai}/K	T_{Ap}/K	T_{AF}/K	T_{Bi}/K	T_{Bp}/K	T_{BF}/K	T_{Ci}/K	T_{Cp}/K	T_{CF}/K	
LLZO	5	437.05	484.66	600.05	501.41	551.71	676.81	611.00	653.22	716.45	0.9943
	10	445.95	493.37	603.75	508.92	560.15	680.89	613.20	660.98	720.23	0.9983
	20	449.45	504.03	604.85	521.75	571.26	690.74	619.23	670.29	724.36	0.9985
	40	460.27	516.64	615.39	529.69	583.26	701.42	623.82	681.82	724.83	0.9990
LLZO-0.1Al	5	441.26	477.87	542.08	478.99	553.35	637.28	598.69	656.15	720.64	0.9940
	10	446.68	486.64	597.55	512.35	561.62	688.63	615.52	661.37	722.68	0.9958
	20	453.39	498.79	605.32	533.37	572.29	693.34	625.40	670.80	726.38	0.9988
	40	456.99	511.26	619.11	545.73	583.99	705.82	629.17	682.76	727.17	0.9990
LLZO-0.2Al	5	442.00	471.32	543.64	483.36	555.18	646.56	598.79	655.54	726.72	0.9890
	10	446.66	481.74	593.33	512.34	567.19	684.53	621.40	661.64	728.85	0.9955
	20	456.95	489.42	597.51	523.15	572.73	689.76	627.01	670.00	730.24	0.9942
	40	466.04	505.14	627.37	546.44	586.61	708.96	632.39	681.46	733.61	0.9991

T_{Xi}: initial temperature of the sub-zone X

T_{XP}: peak temperature of the sub-zone X

T_{XF}: final temperature of the sub-zone X

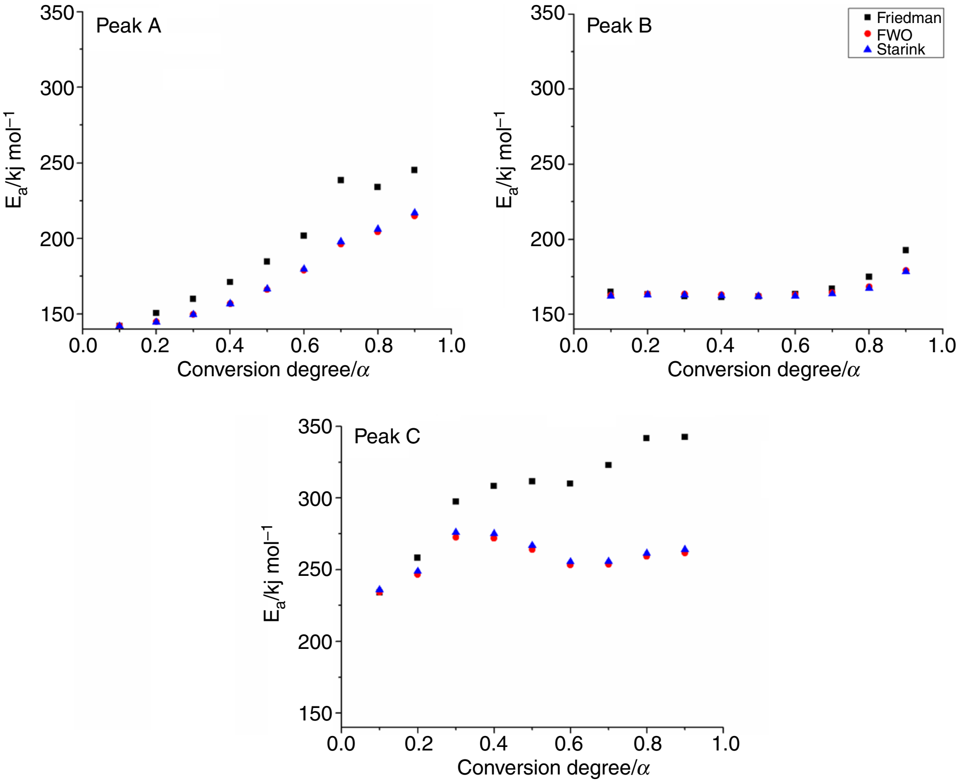

Fig. 5 Activation energy versus conversion dependencies for LLZO

For comparing the activation energy dependency of LLZO using different kinetic models as Friedman, FWO and Starink, vs. conversion for LLZO. Figure 5 was given for sub-regions that show pseudo triple reactions as A, B, C. According to Friedman model, the activation energy values were between 142.1 and 245.3 kJ mol^{-1} with an average value of 192.0 kJ mol^{-1} for the peak zone A of LLZO. The increasing trend in activation energy from initiation to termination was observed in this first pseudo reaction. On the other hand, zone B and C had average activation energy values of 167.9 and 303.0 kJ mol^{-1}, respectively. The other kinetic methods applied as FWO and Starink has shown similar trends in activation energy change of LLZO as it can be seen from Fig. 5. In addition, incorporation of Al to LLZO and its quantity also seemed to affect the reaction kinetics since they led to a change in the characteristics of the material. For a better numerical comparison of the kinetic parameters including activation energy and pre-exponential factor and Table 4 was given for all of the samples. As it can be seen from the table, activation energy of the second and third sub-zone as B and C, was increased with increasing Al content. The reason for this can be attributed to the crystal structure differences of the final residues at higher temperatures. As it was shown in the previous report, when Al atom was introduced in the LLZO lattice, it replaces Li sites by excluding 2 Li atoms and creating lattice voids [20]. Such voids ease atomic movements and diffusion inside the lattice. Accordingly, the dramatic reduction in the average activation energy could be attributed to the Al–Li replacement within the LLZO lattice. Accordingly, the jump in the average activation energy with Al doping may be caused by tetragonal-cubic transformation during these two sub-zones.

Table 4 Calculated kinetic parameters of individual processes of main thermal decomposition zone*

	α	Peak$_A$			Peak$_B$			Peak$_C$		
		E_a/kJ mol^{-1}	R^2	A/s^{-1}	E_a/kJ mol^{-1}	R^2	A/s^{-1}	E_a/kJ mol^{-1}	R^2	A/s^{-1}
LLZO	0.1	142.1	0.9962	7.89×10^{11}	164.9	0.9968	1.50×10^{12}	234.0	0.9923	2.12×10^{15}
	0.2	150.6	0.9936	6.76×10^{12}	163.2	0.9944	1.03×10^{12}	258.3	0.9915	1.94×10^{17}
	0.3	160.0	0.9906	7.01×10^{13}	161.9	0.9915	7.83×10^{11}	297.4	0.9993	2.79×10^{20}
	0.4	171.0	0.9861	1.12×10^{15}	161.4	0.9886	6.95×10^{11}	308.4	0.9981	2.14×10^{21}
	0.5	184.6	0.9787	3.32×10^{16}	161.8	0.9858	7.58×10^{11}	311.6	0.9914	3.88×10^{21}
	0.6	201.7	0.9657	2.33×10^{18}	163.4	0.983	1.09×10^{12}	310.1	0.9919	2.93×10^{21}
	0.7	238.4	0.9423	2.15×10^{22}	167.1	0.9804	2.48×10^{12}	322.9	0.9905	3.19×10^{22}
	0.8	234.1	0.9365	7.24×10^{21}	174.8	0.978	1.33×10^{13}	341.8	0.9900	1.05×10^{24}
	0.9	245.3	0.9806	1.18×10^{23}	192.7	0.9761	6.84×10^{14}	342.7	0.9962	1.23×10^{24}
	$\bar{x}$	192.0		1.63×10^{22}	167.9		7.84×10^{13}	303.0		2.58×10^{23}
LLZO-0.1Al	0.1	136.5	0.9997	2.96×10^{11}	169.5	0.9985	3.77×10^{12}	249.7	0.9962	3.63×10^{16}
	0.2	131.3	0.9915	7.93×10^{10}	192.6	0.9878	5.99×10^{14}	285.4	0.9998	2.72×10^{19}
	0.3	124.6	0.9958	1.44×10^{10}	172.5	0.9880	7.22×10^{12}	316.8	0.9997	9.13×10^{21}
	0.4	118.3	0.9962	2.91×10^{9}	173.7	0.9753	9.55×10^{12}	323.9	0.9986	3.40×10^{22}
	0.5	113.2	0.9951	7.81×10^{8}	188.8	0.9937	2.63×10^{14}	329.9	0.9918	1.03×10^{23}
	0.6	109.2	0.9944	2.82×10^{8}	174.8	0.9926	1.21×10^{13}	332.1	0.9959	1.54×10^{23}
	0.7	111.6	0.9926	5.23×10^{8}	204.1	0.9930	7.55×10^{15}	339.9	0.9962	6.54×10^{23}
	0.8	95.4	0.9936	8.09×10^{6}	210.5	0.9996	3.04×10^{16}	342.9	0.9904	1.15×10^{24}
	0.9	95.1	0.9793	7.64×10^{6}	231.1	0.9990	2.78×10^{18}	343.2	0.9962	1.20×10^{24}
	$\bar{x}$	115.0		4.38×10^{10}	190.9		3.13×10^{17}	318.2		3.67×10^{23}
LLZO-0.2Al	0.1	144.8	0.9999	3.81×10^{12}	180.9	0.9903	3.16×10^{13}	296.9	0.9969	2.23×10^{20}
	0.2	130.4	0.9958	9.22×10^{10}	194.5	0.9946	6.08×10^{14}	313.9	0.9980	5.21×10^{21}
	0.3	133.8	0.9946	2.24×10^{11}	184.5	0.9978	6.92×10^{13}	328.0	0.9999	7.05×10^{22}
	0.4	128.9	0.9900	6.35×10^{10}	180.3	0.9999	2.77×10^{13}	325.7	0.9980	4.66×10^{22}
	0.5	114.2	0.9922	1.41×10^{9}	196.0	0.9979	8.51×10^{14}	324.3	0.9977	3.57×10^{22}
	0.6	110.3	0.9987	5.17×10^{8}	211.3	0.9922	2.35×10^{16}	322.8	0.9985	2.71×10^{22}
	0.7	112.0	0.9965	8.06×10^{8}	229.9	0.9910	1.32×10^{18}	337.6	0.9951	4.18×10^{23}
	0.8	99.7	0.9935	3.34×10^{7}	245.2	0.9907	3.62×10^{19}	333.0	0.9935	1.79×10^{23}
	0.9	101.2	0.9963	4.91×10^{7}	258.0	0.9997	5.74×10^{20}	340.0	0.9973	6.47×10^{23}
	$\bar{x}$	119.5		4.66×10^{11}	209.0		6.80×10^{19}	324.7		1.59×10^{23}

*Calculations were based on Friedman method

In chemical kinetics, the pre-exponential factor is the frequency of collisions between the reactant molecules. When the values of the pre-exponential factor for the Al-free samples were investigated, it can be concluded that intensity of the collisions were enhanced with the increasing temperature. For instance, LLZO presented values of pre-exponential factors between 7.89×10^{11} and 2.58×10^{23} s^{-1}. The changes in the value of the pre-exponential factors by changing conversion degree may be attributed to the variation in reaction chemistry and complex formation [37]. In general, the low value of the pre-exponential factor ($< 10^{9}$ s^{-1}) is known to be related with surface reactions in reaction kinetics. When the reactions are not dependent on surface area, then the low value of pre-exponential factor is accepted to show a tight junctional complex which is considered as a closed complex. On the other hand, the high value of A ($\geq 10^{9}$ s^{-1}) suggests a loose simple complex which is also called as a junctional complex [38]. Also, higher values of pre-exponential factor indicate a greater sensitivity with a reaction temperature range [23]. Clearly, all these changes in the values of the pre-exponential factor also showed that the Al effects on collision frequency of the samples. The values of all pre-exponential factors changed variably in a wide range implying that the composition of Al-free and Al-stabilized LLZO was complex, and complex reactions occurred during the oxidative thermal degradation process. Al incorporation considerably changed the number of collisions and complex formation which were noticeable in different conversion degree values of different pseudo reaction zones.

The linear relationship between the logarithmic form of the pre-exponential factor and the activation energy in order to facilitate the reaction are shown in Fig. 6 to evaluate compensative behavior during oxidative decomposition. The kinetic compensation effect states that there is a linear relationship between ln A and E_a. In other words, a change of the activation energy is noticed, and there will be a shift in the numerical values of pre-exponential factor, which compensates the effect of the activation energy change to some extent in the case of modification of the procedural variables, or to the change of some substituents in a class of similar compounds [39, 40]. The validity of the compensation effect is also considered as a statistical deviation, due to the necessity of extrapolation to calculate the pre-exponential factor. Nevertheless, the significance of the compensation on the kinetic parameters and theoretical interpretations have been supported by several researchers [41–43]. The plots of both Al-free and Al-stabilized samples showed high linearity and regression coefficients were found greater than 0.9990. In other words, a linear relationship between the activation energy and the pre-exponential factor values by an $\ln A = aE_a + b$ type equation can be applicable. The closeness of the regression coefficients to unity shows that, for all heating rates the values of A_α were in accordance

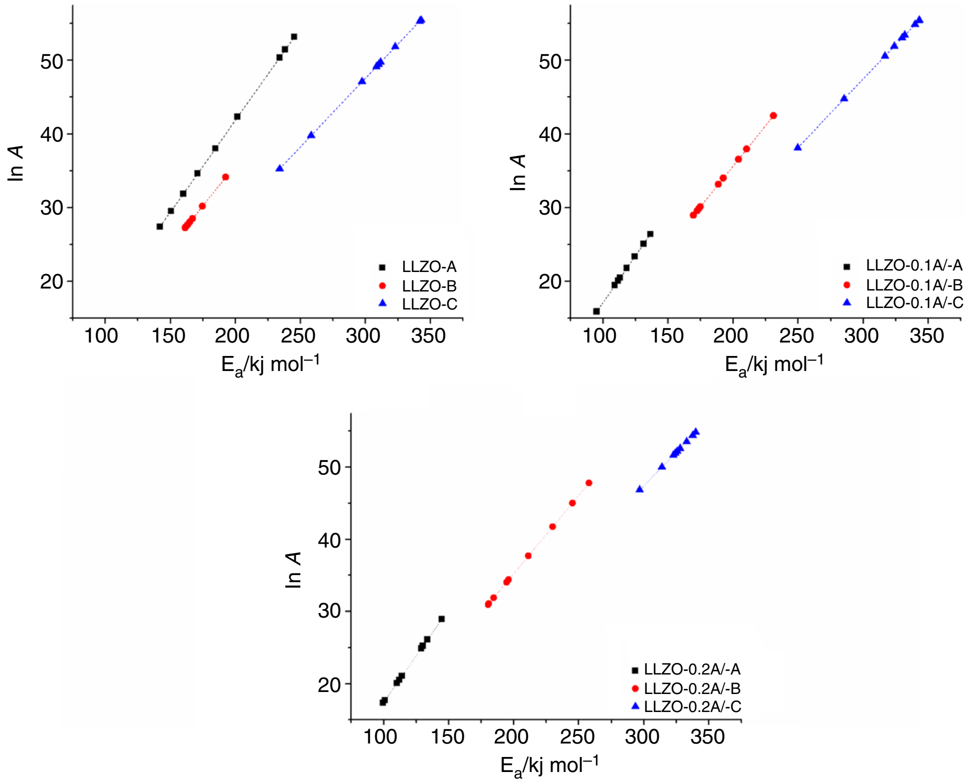

Fig. 6 Plots of logarithmic pre-exponential factor (ln A) versus activation energy (E_a) calculated by Friedman method

with the distributed activation energy for all the stages of the degradation process. There should be energy compensation effect, and the fitting results produced the relationship to be as follows:

$$\ln A = 0.2492E_\mathrm{a} - 7.9784;\ \text{for LLZO} - \text{A} \tag{12}$$

$$\ln A = 0.2204E_\mathrm{a} - 8.1518;\ \text{for LLZO} - \text{B} \tag{13}$$

$$\ln A = 0.1857E_\mathrm{a} - 8.3025;\ \text{for LLZO} - \text{C} \tag{14}$$

$$\ln A = 0.2557E_\mathrm{a} - 8.4695;\ \text{for LLZO} - 0.1\text{Al} - \text{A} \tag{15}$$

$$\ln A = 0.21937E_\mathrm{a} - 8.2011;\ \text{for LLZO} - 0.1\text{Al} - \text{B} \tag{16}$$

$$\ln A = 0.1852E_\mathrm{a} - 8.1204;\ \text{for LLZO} - 0.1\text{Al} - \text{C} \tag{17}$$

$$\ln A = 0.2580E_\mathrm{a} - 8.3901;\ \text{for LLZO} - 0.2\text{Al} - \text{A} \tag{18}$$

$$\ln A = 0.2168E_\mathrm{a} - 8.1327;\ \text{for LLZO} - 0.2\text{Al} - \text{B} \tag{19}$$

$$\ln A = 0.1849E_\mathrm{a} - 8.0428;\ \text{for LLZO} - 0.2\text{Al} - \text{C} \tag{20}$$

Thermodynamic analysis of stabilizer-free and Al-stabilized $Li_7La_3Zr_2O_{12}$

Estimation of thermodynamic parameters allows to determine potential of a process to happen and this indicates favorability and status of the resultant products. This is because the rates of thermal degradation reactions are controlled by the activation energy, the pre-exponential factor and relevant thermodynamic parameters. The parameters including enthalpy change (ΔH/kJ mol^{-1}), Gibbs free energy change (ΔG/kJ mol^{-1}) and entropy change (ΔS/J mol^{-1} K^{-1}) were used to estimate the thermal decomposition behavior of Al-free and Al-incorporated samples. The heating rate of 10 K min^{-1} was selected for the calculation of thermodynamic parameters since a relatively lower heating rate provides more accurate results [44]. The changes in enthalpy, Gibbs free energy and entropy for LLZO are shown in Fig. 7. Likewise, the activation energy values calculated by the Friedman were evaluated for both Al-free and Al-stabilized samples to obtain thermodynamic parameters whose numerical results are summarized in Table 5.

According to the results of the enthalpy change which are also depicted in Fig. 5, the mean enthalpy change of LLZO was found as 187.7 kJ mol^{-1} at sub-zone A while average enthalpy changes of the zone B and C were 163.1 and 297.5, respectively. Enthalpy change indicates the energy differences between the activated complex and the reagents. Positive values of enthalpy change (ΔH) point out that an external energy

Fig. 7 Enthalpy, Gibbs free energy and entropy change variation for LLZO

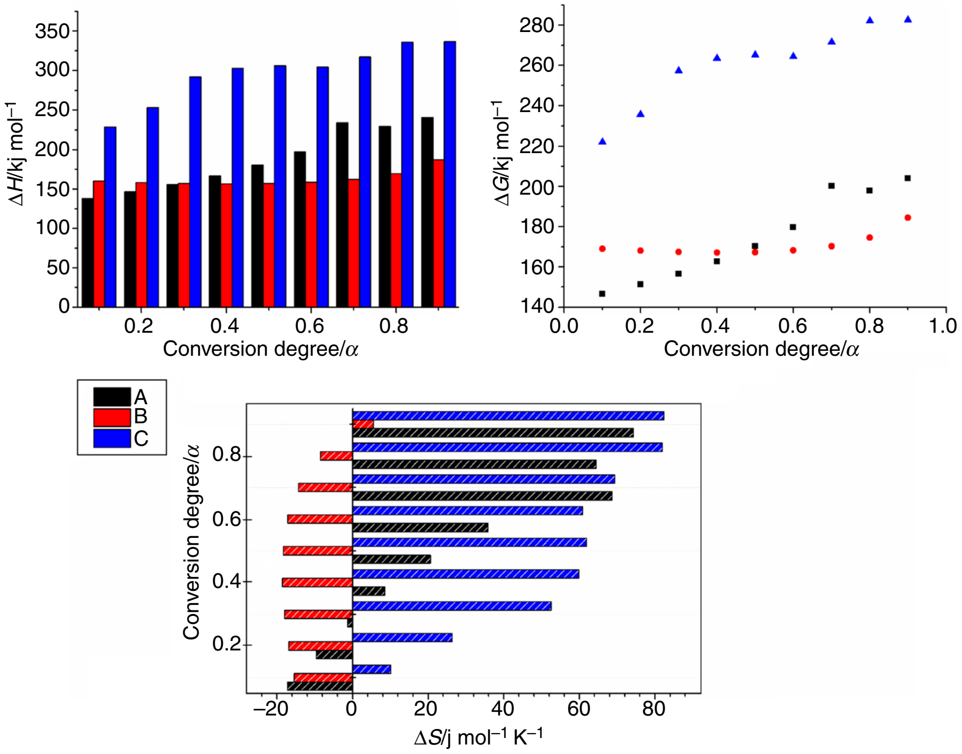

Table 5 Thermodynamic parameters for LLZO and Al-stabilized LLZO samples

	α	$Peak_A$			$Peak_B$			$Peak_C$		
		ΔH/kJ mol^{-1}	ΔG/kJ mol^{-1}	ΔS/J mol^{-1} K^{-1}	ΔH/kJ mol^{-1}	ΔG/kJ mol^{-1}	ΔS/J mol^{-1} K^{-1}	ΔH/kJ mol^{-1}	ΔG/kJ mol^{-1}	ΔS/J mol^{-1} K^{-1}
LLZO	0.1	138.1	146.6	−17.3	160.4	169.0	−15.5	228.7	222.0	10.2
	0.2	146.6	151.4	−9.7	158.6	168.1	−17.0	252.9	235.5	26.3
	0.3	155.9	156.6	−1.3	157.3	167.4	−18.1	291.9	257.3	52.5
	0.4	166.9	162.7	8.5	156.7	167.1	−18.6	302.9	263.4	59.8
	0.5	180.4	170.2	20.6	157.0	167.3	−18.4	306.1	265.2	61.9
	0.6	197.4	179.7	35.8	158.6	168.2	−17.2	304.5	264.4	60.9
	0.7	234.1	200.2	68.6	162.2	170.3	−14.4	317.3	271.5	69.4
	0.8	229.6	197.8	64.5	169.7	174.5	−8.5	336.2	282.1	81.9
	0.9	240.7	204.1	74.3	187.5	184.4	5.5	336.9	282.6	82.4
	$\bar{x}$	187.7	174.4	27.1	163.1	170.7	−13.6	297.5	260.4	56.1
LLZO-0.1Al	0.1	132.6	142.7	−20.8	165.0	171.8	−12.1	244.4	230.9	20.4
	0.2	127.3	139.8	−25.7	188.0	184.6	6.0	280.0	250.8	44.2
	0.3	120.6	136.1	−32.0	167.8	173.4	−10.0	311.3	268.3	65.1
	0.4	114.3	132.7	−37.8	169.0	174.1	−9.1	318.4	272.2	69.8
	0.5	109.1	129.9	−42.7	184.0	182.5	2.7	324.4	275.6	73.7
	0.6	105.1	127.7	−46.4	170.0	174.7	−8.5	326.5	276.8	75.2
	0.7	107.4	129.0	−44.2	199.2	191.0	14.6	334.3	281.2	80.3
	0.8	91.1	120.1	−59.5	205.5	194.6	19.5	337.3	282.9	82.3
	0.9	90.8	120.0	−59.8	226.0	206.0	35.6	337.5	283.0	82.4
	$\bar{x}$	110.9	130.9	−41.0	186.1	183.6	4.3	312.7	269.1	65.9
LLZO-0.2Al	0.1	140.9	146.5	−11.6	176.4	178.9	−4.4	291.5	257.2	51.9
	0.2	126.4	138.5	−25.2	189.9	186.4	6.1	308.5	266.7	63.1
	0.3	129.8	140.4	−22.1	179.8	180.9	−1.9	322.5	274.6	72.5
	0.4	124.8	137.7	−26.7	175.6	178.5	−5.3	320.2	273.3	70.9
	0.5	110.0	129.6	−40.6	191.2	187.3	7.0	318.8	272.5	70.0
	0.6	106.1	127.4	−44.3	206.4	195.8	18.8	317.3	271.7	68.9
	0.7	107.8	128.4	−42.8	225.0	206.1	33.2	332.0	279.9	78.7
	0.8	95.4	121.6	−54.5	240.2	214.6	45.1	327.4	277.4	75.6
	0.9	96.8	122.5	−53.2	252.8	221.8	54.7	334.2	281.3	80.1
	$\bar{x}$	115.3	132.5	−35.7	204.1	194.5	17.0	319.2	272.7	70.2

source is required for product formation [45]. The results of Al-free LLZO indicate that the potential energy barrier of third reaction zone, C, is higher than those occurred lower temperatures.

The average values of enthalpy change were found as 186.1 kJ mol^{-1} and 204.1 kJ mol^{-1} for LLZO-0.1Al and LLZO-0.2Al during reaction zone B, respectively. Moreover, the average enthalpy values increased to 312.7 and 319.2 kJ mol^{-1} during zone C for LLZO-0.1Al and LLZO-0.2Al, respectively. Based on enthalpy change calculations, it's worth to say that the potential energy barrier of LLZO was varied with Al doping and its quantity at the same time. Moreover, small differences between activation energy and enthalpy change showed a low potential barrier between the molecules of the samples, and activated complexes were easier to be formed [46].

When it comes to Gibbs free energy, it is useful to comment on the energy amount which could become available from the decomposition of Al-free and Al-incorporated samples under study. Both thermal decomposition reactions of Al-free and Al-incorporated samples showed positive values of Gibbs free energy as shown in Fig. 7 and Table 5. The numerical values indicated that the thermal decomposition reactions were energetically endergonic and unfavorable during the main degradation zone. Therefore, non-spontaneous processes were driven throughout the main oxidative decomposition range. Furthermore, Al doping caused an increase in the mean values of Gibbs free energy change during stage B and C.

As illuminated in Fig. 7, entropy change with respect to the conversion degree was plotted to conclude the disorder of the Al-free LLZO system. It is well known that negative entropy change shows that the material has gone through a chemical process that brought it close to a state of thermodynamic equilibrium since it was related to the formation of activated complex species [47]. During early stages of sub-zone A of LLZO, entropy change was negative while it is positive after a conversion degree of 0.4. To put it in other words, the transition state had a more ordered structure than the reactants in the ground state at the early stages of conversion of LLZO. A negative value in entropy change declares that the disorder of the system decreases as the reaction proceeds [48]. The whole process during reaction zone of A and C resulted in positive average entropy change values for LLZO. The average entropy change values of all samples indicated that it was related to the presence of Al in the LLZO matrix and amount of the Al doped.

Conclusions

The data for the thermal decomposition kinetics and thermodynamics of Al-free and Al-stabilized LLZO xerogels based on TGA are first time reported in this paper. The findings of the study provide useful technical information that may guide researchers for providing a better understanding on Pechini based LLZO systems and optimization of industrial LLZO xerogels for solid-state battery implementations. The kinetic data calculated through different non-isothermal model-free methods were shown to be consistent among themselves which may simulate the oxidative thermal decomposition process. Iso-conversional analysis and dTG peak analysis showed that oxidative decomposition process of Al-free and Al-stabilized LLZO is a rather complex process that includes multiple stages with overlapping peaks. An analytical peak deconvolution approach was adopted to main thermal degradation zone and three sub-zones were identified. Remarkable difference of thermal degradation behavior, kinetics and thermodynamics between Al-free and Al-stabilized samples was obtained and results have revealed that Al incorporation functions on widening the main decomposition zone and on changing activation energy, pre-exponential factor and thermodynamic parameters as changes in enthalpy, entropy and Gibbs free energy. The change characteristics of these kinetic and thermodynamic parameters supported the complex reaction schemes during the oxidative thermal decomposition process of the samples.

Acknowledgements The study was funded by Eskisehir Technical University Scientific Research Projects Unit with a grant number of 1802F030. Authors would also like to thank Prof. Dr. Ender Suvacı and Dr. Tümerkan Kesim for their valuable support on TGA analysis. Data collection and analysis were performed by Dr. Kamil Burak Dermenci and Dr. Gamzenur Özsin. Writing review and editing were performed by Prof. Dr. Servet Turan. All authors read and approved the final manuscript.

Compliance with ethical standards

Conflict of interest The authors declare that they have no conflict of interest.

References

1. Wu F, Maier J, Yu Y. Guidelines and trends for next-generation rechargeable lithium and lithium-ion batteries. Chem Soc Rev. 2020;49:1569–614.
2. Fan E, Li L, Wang Z, Lin J, Huang Y, Yao Y, et al. Sustainable recycling technology for Li-ion batteries and beyond: challenges and future prospects. Chem Rev. 2020;120:7020–63.
3. Scrosati B, Garche J. Lithium batteries: status, prospects and future. J Power Sources. 2010;195:2419–30.
4. Arbizzani C, Gabrielli G, Mastragostino M. Thermal stability and flammability of electrolytes for lithium-ion batteries. J Power Sources. 2011;196:4801–5.
5. Liu H, Wei Z, He W, Zhao J. Thermal issues about Li-ion batteries and recent progress in battery thermal management systems: A review. Energy Convers Manag. 2017;150:304–30.

6. Kalhoff J, Eshetu GG, Bresser D, Passerini S. Safer electrolytes for lithium-ion batteries: state of the art and perspectives. Chemsuschem. 2015;8:2154–75.
7. Sun Y-K, Myung S-T, Park B-C, Prakash J, Belharouak I, Amine K. High-energy cathode material for long-life and safe lithium batteries. Nat Mater. 2009;8:320–4.
8. Thangadurai V, Narayanan S, Pinzaru D. Garnet-type solid-state fast Li ion conductors for Li batteries: critical review. Chem Soc Rev. 2014;43:4714.
9. Jin Y, McGinn PJ. Li7La3Zr2O12 electrolyte stability in air and fabrication of a Li/Li7La3Zr2O12/Cu0.1V2O5 solid-state battery. J Power Sources. 2013;239:326–31.
10. Thompson T, Wolfenstine J, Allen JL, Johannes M, Huq A, David IN, et al. Tetragonal vs. cubic phase stability in Al–free Ta doped Li7La3Zr2O12 (LLZO). J Mater Chem A. 2014;2:13431–6.
11. Allen JL, Wolfenstine J, Rangasamy E, Sakamoto J. Effect of substitution (Ta, Al, Ga) on the conductivity of Li7La3Zr2O12. J Power Sources. 2012;206:315–9.
12. El Shinawi H, Janek J. Stabilization of cubic lithium-stuffed garnets of the type "Li7La3Zr2O12" by addition of gallium. J Power Sources. 2013;225:13–9.
13. Rettenwander D, Geiger CA, Amthauer G. Synthesis and Crystal Chemistry of the Fast Li-Ion Conductor Li7La3Zr2O12 Doped with Fe. Inorg Chem. 2013;52:8005–9.
14. Rangasamy E, Wolfenstine J, Sakamoto J. The role of Al and Li concentration on the formation of cubic garnet solid electrolyte of nominal composition Li7La3Zr2O12. Solid State Ionics. 2012;206:28–32.
15. Cao Z, Wu W, Li Y, Zhao J, He W, Liu J, et al. Lithium ionic conductivity of Li7-3xFexLa3Zr2O12 ceramics by the Pechini method. Ionics. 2020;26:4247–56.
16. Shen F, Guo W, Zeng D, Sun Z, Gao J, Li J, et al. A Simple and Highly Efficient Method toward High-Density Garnet-Type LLZTO Solid-State Electrolyte. ACS Appl Mater Interfaces. 2020;12:30313–9.
17. Ahn JH, Park S-Y, Lee J-M, Park Y, Lee J-H. Local impedance spectroscopic and microstructural analyses of Al-in-diffused Li7La3Zr2O12. J Power Sources. 2014;254:287–92.
18. Chen R-J, Huang M, Huang W-Z, Shen Y, Lin Y-H, Nan C-W. Effect of calcining and Al doping on structure and conductivity of Li 7 La 3 Zr 2 O 12. Solid State Ionics. 2014;265:7–12.
19. Dermenci KB, Çekiç E, Turan S. Al stabilized Li7La3Zr2O12 solid electrolytes for all-solid state Li-ion batteries. Int J Hydrog Energy. 2016;41:9860–7.
20. Dermenci KB, Turan S. Structural insights on understanding the cubic phase stabilization mechanism of sol–gel synthesized Li7-3xAlxLa3Zr2O12 (x = 0–0.4): The effect of ZrOCl2 and ZrO(NO3)2. Ceram Int. 2018;44:11852–7.
21. Chowdhury A, O'Callaghan S, Skidmore TA, James C, Milne SJ. Nanopowders of Na 0.5 K 0.5 NbO 3 prepared by the Pechini method. J Am Ceram Soc. 2009;92:758–61.
22. Rojek B, Wesolowski M. Compatibility study of theophylline with excipients using thermogravimetry supported by kinetic analysis. J Therm Anal Calorim. 2020;120:7020–63.
23. Qureshi U, Imtiaz B, Jamal Y. Synthesizing PET and food waste into refuse plastic fuel (RPF): optimization and kinetic modeling. J Therm Anal Calorim. 2019;140:1745–58.
24. Granado L, Tavernier R, Foyer G, David G, Caillol S. Comparative curing kinetics study of high char yield formaldehyde- and terephthalaldehyde-phenolic thermosets. Thermochim Acta. 2018;667:42–9.
25. Das P, Tiwari P. Thermal degradation kinetics of plastics and model selection. Thermochim Acta. 2017;654:191–202.
26. Vyazovkin S, Burnham AK, Criado JM, Pérez-Maqueda LA, Popescu C, Sbirrazzuoli N. ICTAC Kinetics Committee recommendations for performing kinetic computations on thermal analysis data. Thermochim Acta. 2011;520:1–19.
27. Friedman HL. Kinetics of thermal degradation of char-forming plastics from thermogravimetry. Application to a phenolic plastic. J Polym Sci Part C Polym Symp. 2007;6:183–95.
28. Flynn JH, Wall LA. General treatment of the thermogravimetry of polymers. J Res Natl Bur Stand Sect A Phys Chem. 1966;70A:487–523.
29. Ozawa T. A new method of analyzing thermogravimetric data. Bull Chem Soc Jpn. 1965;38:1881–6.
30. Starink MJ. A new method for the derivation of activation energies from experiments performed at constant heating rate. Thermochim Acta. 1996;288:97–104.
31. Awasthi A, Dhyani V, Biswas B, Kumar J, Bhaskar T. Production of phenolic compounds using waste coir pith: estimation of kinetic and thermodynamic parameters. Bioresour Technol. 2019;274:173–9.
32. Sharma P, Pandey OP, Diwan PK. Non-isothermal kinetics of pseudo-components of waste biomass. Fuel. 2019;253:1149–61.
33. Afyon S, Krumeich F, Rupp JLM. A shortcut to garnet-type fast Li-ion conductors for all-solid state batteries. J Mater Chem A. 2015;3:18636–48.
34. Li H, Liu F, Ma X, Cui P, Gao Y, Yu M, et al. Effects of biodiesel blends on the kinetic and thermodynamic parameters of fossil diesel during thermal degradation. Energy Convers Manag. 2019;198:111930.
35. Kok MV, Varfolomeev MA, Nurgaliev DK. Low-temperature oxidation reactions of crude oils using TGA–DSC techniques. J Therm Anal Calorim. 2019;141:775–81.
36. Carrier M, Auret L, Bridgwater A, Knoetze JH. Using apparent activation energy as a reactivity criterion for biomass pyrolysis. Energy Fuels. 2016;30:7834–41.
37. Mehmood MA, Ahmad MS, Liu Q, Liu CG, Tahir MH, Aloqbi AA, et al. Helianthus tuberosus as a promising feedstock for bioenergy and chemicals appraised through pyrolysis, kinetics, and TG–FTIR–MS based study. Energy Convers Manag. 2019;194:37–45.
38. Ma J, Luo H, Li Y, Liu Z, Li D, Gai C, et al. Pyrolysis kinetics and thermodynamic parameters of the hydrochars derived from co-hydrothermal carbonization of sawdust and sewage sludge using thermogravimetric analysis. Bioresour Technol. 2019;282:133–41.
39. Zsakó J. The kinetic compensation effect. J Therm Anal. 1976;9:101–8.
40. Janković B. The pyrolysis of coffee paper cup waste samples using non-isothermal thermo-analytical techniques. The use of combined kinetic and statistical analysis in the interpretation of mechanistic features of the process. Energy Convers Manag. 2014;85:33–49.
41. Uzun BB, Yaman E. Pyrolysis kinetics of walnut shell and waste polyolefins using thermogravimetric analysis. J Energy Inst. 2017;90:825–37.
42. Jia C, Chen J, Bai J, Yang X, Song S, Wang Q. Kinetics of the pyrolysis of oil sands based upon thermogravimetric analysis. Thermochim Acta. 2018;666:66–74.
43. Galwey AK, Mortimer M. Compensation effects and compensation defects in kinetic and mechanistic interpretations of heterogeneous chemical reactions. Int J Chem Kinet. 2006;38:464–73.
44. Chong CT, Mong GR, Ng J-H, Chong WWF, Ani FN, Lam SS, et al. Pyrolysis characteristics and kinetic studies of horse manure using thermogravimetric analysis. Energy Convers Manag. 2019;180:1260–7.
45. Mumbach GD, Alves JLF, Da Silva JCG, De Sena RF, Marangoni C, Machado RAF, et al. Thermal investigation of plastic solid waste pyrolysis via the deconvolution technique using the asymmetric double sigmoidal function: Determination of the

kinetic triplet, thermodynamic parameters, thermal lifetime and pyrolytic oil composition for clean. Energy Convers Manag. 2019;200:112031.

46. Fong MJB, Loy ACM, Chin BLF, Lam MK, Yusup S, Jawad ZA. Catalytic pyrolysis of *Chlorella vulgaris*: kinetic and thermodynamic analysis. Bioresour Technol. 2019;289:121689.
47. Tiong YW, Yap CL, Gan S, Yap WSP. Kinetic and thermodynamic studies of oil palm mesocarp fiber cellulose conversion to levulinic acid and upgrading to ethyl levulinate via indium trichloride-ionic liquids. Renew Energy. 2020;146:932–43.
48. Ding G, He B, Yao H, Cao Y, Su L, Duan Z. Co-combustion behaviors of municipal solid waste and low-rank coal semi-coke in air or oxygen/carbon dioxide atmospheres. J Therm Anal Calorim. 2019. https://doi.org/10.1007/s10973-019-09170-z.